Akademie věd
České republiky

Teze disertace
k získání vědeckého titulu "doktor věd"
ve skupině věd chemických

Computational Exploration of Endohedral Fullerenes: From Spectroscopic Properties to Molecular Electronics

Komise pro obhajoby doktorských disertací v oboru **Fyzikální chemie**

Jméno uchazeče **Michal Straka**

Pracoviště uchazeče: **Ústav organické chemie a biochemie**

Místo a datum: **Praha, 5. listopad 2025**

Summary

This dissertation presents a comprehensive computational investigation of the chemistry and physics of endohedral fullerenes. The research narrative progresses from foundational studies of their electronic and spectroscopic properties, using encapsulated noble gases as spectroscopic probes, to the exploration of exotic chemical bonding phenomena within the fullerene nanospace, particularly focusing on actinide-actinide interactions. This fundamental understanding is then extended in the rational design of novel molecular-scale devices. We detail the conceptualization and *in silico* validation of electric field-driven fullerene molecular switches, which function as molecular memristors controlled by external electric fields. Finally, we introduce the concept of a 'spinristor,' a unique component with no macroscopic analogue, which combines memristive switching with spin-filtering capabilities. This work also highlights the evolution of computational methodologies required to accurately model these complex systems and underscores the potential of endohedral fullerenes as building blocks for next-generation nanotechnology.

1. Introduction

1.1 Fullerenes

Since the discovery of Buckminsterfullerene (C_{60}) in 1985,[1] fullerenes, closed-cage molecules composed entirely of carbon atoms, have strongly attracted the scientific community.[2–4] These unique structures, comprising interconnected carbon pentagons and hexagons, are more than just a distinct allotrope of carbon. The most important feature of fullerenes is their internal **cavity**, a void that can encapsulate other atoms, ions, clusters, or small molecules, giving rise to a class of compounds known as endohedral fullerenes (EFs), endohedral metallofullerenes (EMFs), and clusterfullerenes (CFs).[2] Denoted with the @ symbol, e.g., He@C_{60}, these host-guest systems represent unique molecules, where the encapsulated species are studied under conditions of confinement, isolated from external intermolecular interactions.

The synthesis of endohedral fullerenes is typically achieved under high-energy conditions, such as in an **electric arc** between graphite electrodes or through **laser ablation** of a graphite surface.[2,5] By introducing metals, metal oxides, or metal compounds into this environment, guest species can be trapped within the forming carbon cages. While these methods have enabled the production of a large family of endohedral fullerenes containing noble gases, alkali metals, early d-metals, lanthanides, and even actinides, the process often yields a complex mixture of different fullerene cages and isomers, necessitating sophisticated separation techniques such as **high-performance liquid chromatography** (HPLC) for purification.[2] More recently, multi-step ***fullerene surgery*** techniques have emerged, allowing for the precise opening of a fullerene cage, insertion of a guest molecule, and subsequent closing of the cage orifice.[6]

1.2. The Fullerene Cage as a Nanolaboratory

The central premise of this dissertation is that the fullerene cage is not a passive container but an active participant in the chemistry and physics it hosts. The endohedral environment serves as a unique '**nanolaboratory**' where the fundamental properties of matter can be explored under novel boundary conditions. The confinement profoundly influences the spectroscopic signatures of the encapsulated guests, providing a sensitive tool to probe the electronic and magnetic properties of the cage itself.[7] Furthermore, the steric constraints and electronic environment within the cage can stabilize otherwise fleeting species and facilitate the formation of **unprecedented chemical bonds.**[8,9] This dual role—where the guest probes the host and the host modifies the guest—opens avenues for both fundamental discovery and the **rational design of functional molecular materials**. The potential applications of endohedral fullerenes are diverse, spanning materials science (e.g., superconductors, solar cells),[10] medicine (e.g., MRI contrast agents),[11] and **molecular electronics**.[12,13]

1.3. Research Trajectory and Dissertation Outline

This dissertation documents a computational research journey progressing from fundamental inquiry to applied design in twenty-three published original works. The narrative is structured to demonstrate how we proceeded from a deeper understanding of the basic physics and chemistry

of endohedral systems, gained through advanced computational modeling, to the engineering of novel molecular-scale devices. The thesis is organized as follows:

- **Chapter 2: Research Methods.** This chapter briefly maps the theoretical methodology used in this thesis.
- **Chapter 3: Spectroscopic Probes of Endohedral Environment.** This chapter details the use of encapsulated noble gas atoms (^{3}He and ^{129}Xe) as highly sensitive NMR probes to map the electronic and magnetic landscape inside a fullerene cage. It highlights the evolution of computational methods required to accurately reproduce and interpret experimental spectra, revealing the critical roles of cage symmetry, relativity, and dynamics (**Papers 1–9**). Moreover, we show how magnetic circular dichroism-based spectroscopies extend the opportunities of detection of fullerene compounds (**Papers 10–12**).
- **Chapter 4: Unveiling Exotic Chemical Bonding in Fullerene Cages.** Here, the focus shifts to the chemistry *enabled* by the endohedral environment. This chapter explores novel host-guest interactions, including charge-transfer bonding phenomena and rarely detected actinide-actinide bonds (**Papers 13–19**). It underscores the importance of methodological rigor and scientific self-correction in computational chemistry, showing how initial theories were refined by higher-level calculations (**Paper 16**). An example of 'molecular crystal' $F_2^-@C_{60}^+$ is discussed (**Paper 17**).
- **Chapter 5: Rational Design of Fullerene-Based Molecular Electronics.** This section details the conceptualization and *in silico* design of a fullerene memristor (**Papers 20–23**). This molecular memristor operates by controlling the orientation of an encapsulated polar molecule with an external electric field, a process modeled through a complete rational design cycle from concept to the derivation of engineering rules. It introduces the spinristor, a novel device with no macroscopic analogue that integrates memristive switching with spin-filtering capabilities (**Paper 22**).

2. Research Methodology

The research presented herein relies on a pragmatic and hierarchical application of state-of-the-art computational tools, carefully selected to match the physical complexity of the problem at hand.

2.1. Quantum Chemical Methods

The electronic structure of fullerene systems is described using a range of quantum chemical methods. For many systems exhibiting a well-behaved, single-reference ground state, **Density Functional Theory (DFT)** provides a computationally efficient and often reliable framework for geometry optimization and property calculation. A wide variety of functionals, spanning the generalized gradient approximation (**GGA**), **meta-GGA**, and **hybrid** functionals, are employed. For higher accuracy, particularly for energetics and weak interactions, *ab initio* wavefunction-based methods are utilized, including **Møller-Plesset perturbation theory** to the second order (**MP2**), also in its spin-component-scaled (**SCS-MP2**) variant, and the 'gold standard' **Coupled Cluster** (**CC**) theory, with single, double, and non-iterative triple excitations, **CCSD(T)**, sometimes in approximative **DLPNO** (**Domain-based Local Pair Natural Orbital**) mode. For electronically the most intriguing endohedral fullerenes with di-actinides, **multireference methods** are essential. These include the **Complete Active Space Self-Consistent Field** (**CASSCF**) in combination with second-order perturbation theory (**CASPT2**).

2.2. Relativistic Effects

When studying systems containing heavy elements, such as xenon and actinides, the relativistic effects must be included. In heavy atoms, the high nuclear charge causes the inner-shell electrons to move at speeds approaching the speed of light, leading to significant relativistic contraction of s- and p-orbitals, expansion of d- and f-orbitals, and strong spin-orbit coupling. These effects may profoundly alter chemical bonding and spectroscopic properties. A spectrum of relativistic methods was used to capture these effects. The simplest approach involves replacing the inner-shell electrons with **Effective Core Potentials (ECPs)**, which implicitly include scalar relativistic effects. For more quantitative accuracy, explicit

two-component methods such as the **Zeroth-Order Regular Approximation (ZORA)**, often including **spin-orbit coupling** (**SO-ZORA**) are employed. Perturbative approaches like the **Breit-Pauli Perturbation Theory (BPPT)** have been used for calculating magnetic resonance properties.

2.3. Molecular Dynamics

Some properties of endohedral fullerenes are affected by the complex motion of the guest within the host cage and the vibrations of the cage itself. To capture these effects, **Molecular Dynamics (MD)** simulations are indispensable. **Classical MD**, using parameterized force fields, was employed to simulate the behavior of large systems over long timescales, such as a fullerene solvated in a periodic box of solvent molecules. For cases where the electronic structure of the guest-host system is critical to the dynamics, the more computationally demanding **Ab Initio Molecular Dynamics (AIMD)** is used.

2.4. A Unified Methodological Philosophy

An important point of the work presented is the careful calibration of computationally efficient methods (like DFT) against more accurate, high-level *ab initio* calculations or, when available, against experimental data. This approach ensures the reliability of the chosen methods for the specific problem being investigated. Furthermore, the work demonstrates a sophisticated understanding of the appropriate level of theory required for different physical phenomena. For instance, while calibrated DFT proves sufficient for predicting ^{3}He NMR shifts in diamagnetic fullerenes (**Chapter 3**), it is shown to be fundamentally unreliable for describing the spin-state energetics and quantitative bonding in di-actinide systems (**Chapter 4**), where only computationally expensive multireference methods provide a credible picture. In yet another case, the simulation of ^{129}Xe NMR shifts (**Chapter 3**), no single method is adequate. Instead, a multi-scale protocol combining MD, relativistic quantum chemistry, and explicit solvent models is required to achieve agreement with experiment.

3. Spectroscopic Probes of Endohedral Environment

3.1. ^{3}He NMR: A Sensitive Probe of Fullerene Cage and Its Electronic Structure

The encapsulation of a noble gas atom within a fullerene provides an exceptionally interesting system for studying fullerenes.[7,14] The noble gas, being chemically inert, does not form covalent bonds with the cage wall, meaning its spectroscopic properties are determined solely by the physical and electronic environment imposed by the host. The ^{3}He nucleus is an ideal nuclear magnetic resonance (NMR) probe. Experimentally, ^{3}He atom can be inserted in a fullerene cage using high pressure and elevated temperature.[15] Its NMR chemical shift, $\delta(^3\text{He})$, is sensitive to its surroundings, exhibiting an unprecedentedly large range in endohedral helium fullerenes (EHFs), spanning from approximately −50 ppm to 10 ppm relative to the free He atom.[18] This sensitivity makes $\delta(^3\text{He})$ a powerful fingerprint for identifying different fullerene cages, distinguishing between isomers of the same cage, and detecting changes in the cage's electronic structure, such as those induced by charging or external derivatization.

In 2005, we asked ourselves a central question: Can we accurately reproduce $\delta(^3\text{He})$ signals in helium fullerenes by theoretical calculations to help the experiment in distinguishing among various fullerenes via ^{3}He NMR? In method calibration **Papers 1–2,** we documented that DFT is capable of accurate description of the geometries and ^{3}He NMR shifts in helium fullerenes. Functionals, such as BP86 and BHandHLYP, combined with flexible triple-zeta basis sets (def-TZVP), were shown to provide quantitative agreement with experimental data, often predicting $\delta(^3\text{He})$ values to within a few ppm of accuracy (**Figure 3.1**), which is sufficient for distinction among various EHFs and among their isomers. With calibrated methodology we were able to almost fully interpret ^{3}He spectrum of a mixture of EHFs[16] and identify which cages are responsible for observed signals (**Paper 2**). Based on calculations, we were even able to point out wrong experimental assignment of individual peaks[17] (**Paper 1**).
With the calibrated methodology we could solve a complex puzzle that emerged from the experimental studies of EHFs.[17]

Why are the δ(^{3}He) values in helium fullerenes so large in magnitude? Why they differ so substantially among isomers of rather similar cages?

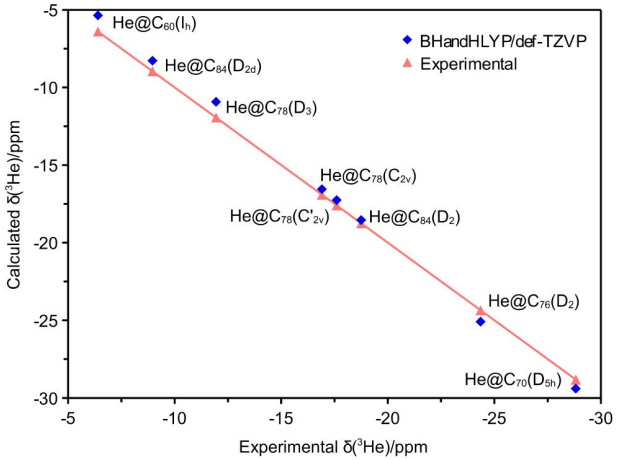

(a)

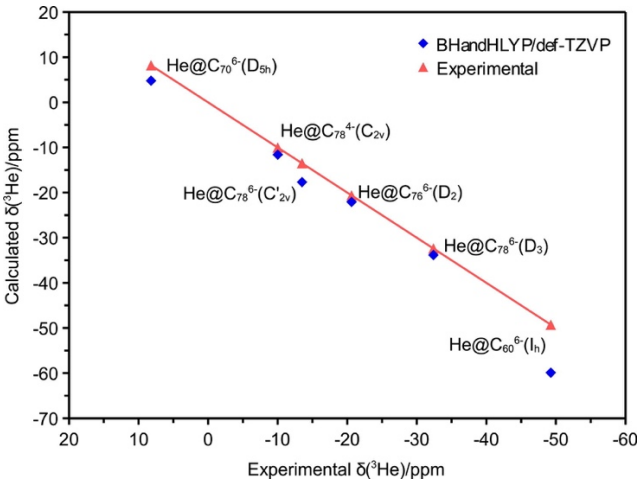

(b)

Figure 3.1: Calculated (blue) vs experimental (red) ^{3}He chemical shifts in **(a)** neutral and **(b)** hexaanionic helium fullerenes. Adopted from **Paper 2**.

Why they change abruptly upon charging the fullerene cage (**Figure 3.1)**? These step changes can be illustrated e.g. on ^{3}He@C_{60} and ^{3}He@C_{70} and their hexaanions in **Figure 3.1**. The experimental values of –6.4 and –28.8 ppm in neutral ^{3}He@C_{60} and ^{3}He@C_{70} exhibit dramatic and diametrically opposed changes in their δ(^{3}He) values. The ^{3}He nucleus becomes strongly shielded upon charging in He@C_{60}^{6-} with δ(^{3}He) = –49.3 ppm while the ^{3}He nucleus in He@C_{70}^{6-} is deshielded, with δ(^{3}He) = 8.2 ppm, **Figure 3.1**. This counterintuitive result, that adding six electrons can lead to either additional shielding or additional deshielding, cannot be explained by classical simple electron density arguments, as usually done in NMR science.

In **Paper 3** we demonstrated that the solution of this puzzle lies in the fundamental theory of NMR shielding and the profound influence of molecular symmetry. In theory, the total isotropic nuclear magnetic shielding constant, σ, can be decomposed into a diamagnetic term, σ_d, and a paramagnetic term, σ_p with $\sigma = \sigma_d + \sigma_p$. The diamagnetic term, σ_d, is always positive (shielding) and is directly related to the electron density around the nucleus. Adding electrons to the fullerene cage leads to an increase in σ_d. The paramagnetic term, σ_p, arises from second-order effects involving orbital magnetic couplings (OMCs) between individual occupied and virtual molecular orbitals (described as MO↔MO* in following) and is negative (deshielding).

The symmetry rules dictate, that some of these possible couplings are symmetry forbidden and do not contribute at all. The high symmetry of the fullerene cages is then the master variable that controls the magnitude of the paramagnetic term and, consequently, the abrupt differences in δ(^{3}He) among fullerene cages and their isomers as well as among different charge states of a cage. Because the inverse dependence of OMCs on the energy gap between orbitals, the effect boils down to the frontier orbitals as illustrated in **Figure 3.2** with main OMCs in different charge states of He@C_{60}:

- **In neutral He@C_{60}** the cage-based $6h_u$ HOMO gives rise to a huge paramagnetic deshielding via symmetry-allowed coupling with $7t_{1u}$ and $7t_{2u}$ virtual MOs (ca. –50 and –18 ppm to total ^{3}He shift),

Figure 3.2. This effect cancels the diamagnetic shielding giving rise to the experimental ^{3}He shift of –6.4 ppm.

- **In He@C_{60}^{6-}**, six added electrons populate $7t_{1u}$ which quenches the $6h_{1u}\leftrightarrow 7t_{1u}$ OMC contribution. The $7t_{1u}$ that is now HOMO does not have a proper symmetry allowed partner to couple with, and thus adding electrons to the cage makes the He atom more shielded, $\delta(^3\text{He})_{exp} \sim -49.3$ ppm.
- **In He@C_{60}^{10+}**, however, the removal of ten $6h_{1u}$ electrons quenches both deshielding contributions leading to predicted $\delta(^3\text{He})_{exp} \sim -86$ ppm. Here, removing electrons leads to additional shielding.
- Similarly, adding electrons to He@C_{70} introduces additional paramagnetic deshielding that compensates the effect of diamagnetic shielding and adding the electrons thus induces large deshielding. Details can be found in **Paper 3**.

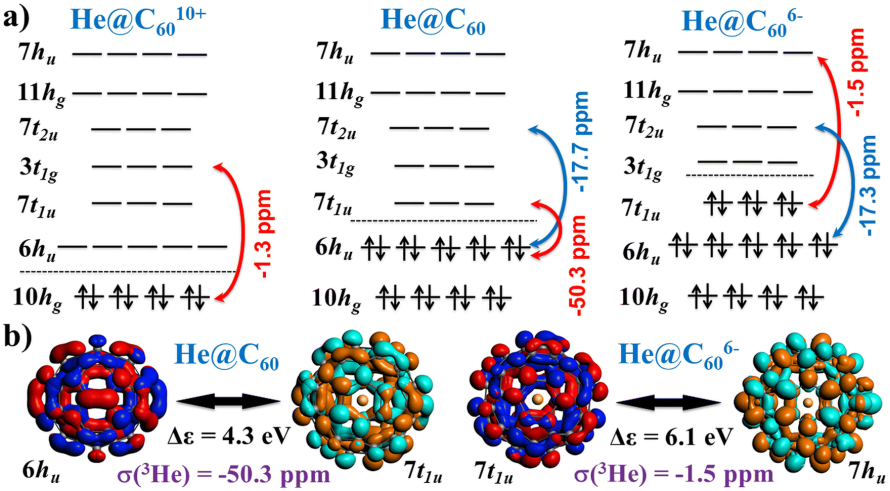

Figure 3.2: (a) Frontier molecular orbitals of He@C_{60}^{10+}, He@C_{60}, and He@C_{60}^{6-} **(b)** the most contributing OMCs in He@C_{60} (left), and He@C_{60}^{6-} (right). Adopted from **Paper 3.**

This explanation reveals that the unexpectedly broad/large range and non-intuitive behavior of $\delta(^3\text{He})$ shifts in EHFs are direct consequences of the

cage symmetry, which acts as a switch, either quenching or allowing large paramagnetic contributions from the frontier orbitals upon changes in the cage's electronic structure. Notably, this argumentation can be applied to other He fullerenes observed experimentally so far.

3.2. The Challenge of Xe@C60 : Simulating Experimental Conditions for Calculations of 129Xe NMR in Confined Xe Systems

Xe atom is an excellent NMR probe. Owing to its inertness, Xe gas can be pumped into different materials, such as microporous and mesoporous systems, liquids, clathrates, or clusters without reacting chemically, to investigate their microscopic structure and properties using ^{129}Xe NMR spectroscopy.[18,19]

Our contribution in this field was to establish methodology for calculations of ^{129}Xe NMR shifts in confined Xe systems using Xe atom and Xe@C_{60} fullerene solvated in benzene as model systems (**Papers 4–6**). While static DFT models proved successful for predicting ^{3}He chemical shifts (**Chapter 3.1**) extending this approach to heavier ^{129}Xe revealed the limitations of the methodology and necessitated a more sophisticated computational protocol. The Xe atom, with its large and highly polarizable electron cloud, is extremely sensitive to its environment, but accurately modeling this sensitivity requires accounting for various physical effects that are not critical for helium atom.

A systematic, piecewise investigation was required to build a physically sound model capable of achieving the right result for the right reasons in modelling ^{129}Xe NMR shifts in confined Xe systems. This was shown on model Xe@C_{60} molecule (**Papers 4-5**) and on Xe atom dissolved in benzene (**Paper 6**). Three essential contributions must be included for an accurate simulation of ^{129}Xe NMR parameters in confined Xe systems:

1. **Electron Correlation Effects**: Initial studies of single-geometry Xe@C_{60} *in vacuo* at 0K revealed critical dependence of calculated ^{129}Xe shift on the DFT functional. Unfortunately, the predicted shifts varied by several hundreds of ppm. Thus, for effective simulations of ^{129}Xe chemical shifts, we calibrated DFT against accurate CCSD(T) calculations on a Xe-benzene model systems.

For such calculations the DFT BHandHLYP functional mimicked well the CCSD(T) results and BHandHLYP was used as workhorse functional in further studies (**Paper 4**).

2. **Relativistic Effects:** Due to the high nuclear charge of Xe atom, relativistic effects on its electron cloud are substantial. Relativistic effects were included using Breit-Pauli Perturbation Theory (BPPT) at the DFT level. The calculations showed that relativity provides a large, positive (deshielding) contribution to the Xe chemical shift, accounting for approximately 8% of the total value (ca. 14 ppm in Xe@C_{60}, **Figure 3.3**, **Papers 4–6**).
3. **Cage Dynamics:** Even by employing calibrated DFT level and BPPT-derived relativistic effects we were not able to reproduce the experiment using static geometry. At experimental temperatures, both the encapsulated Xe atom and the host C_{60} cage are in constant motion. To capture these effects, *ab initio* molecular dynamics (AIMD) simulations were performed. The analysis revealed that the 'rattling' motion of the Xe atom within a static, rigid cage has a negligible effect on the time-averaged chemical shift (~0.5 ppm). The thermal vibrations and deformations of the fullerene cage itself, however, cause more significant fluctuations in the shielding environment. Cage dynamics adds another positive contribution to $\delta(^{129}Xe)$, accounting for roughly 7% (ca. 12 ppm in Xe@C_{60}) of the total ^{129}Xe chemical shift (**Figure 3.3, Papers 4–5**).
4. **Explicit Dynamic Solvent Effects:** However, even adding the cage dynamics of the Xe@C_{60} was yet not enough to reproduce the experimental numbers. We have revealed that the dynamic fluctuations of the surrounding solvent molecules must be included to describe the $\delta(^{129}Xe)$ correctly (**Papers 5–6**). Initial attempts to model solvent effects using implicit continuum solvent models failed to capture any significant effect. Performing large-scale MD simulations of a Xe@C_{60} molecule embedded in a periodic box of explicit benzene molecules and averaging the calculated ^{129}Xe NMR shielding over snapshots of MD that included the first solvation shell of benzene molecules contributed additional ca. 7% (12 ppm) to the final calculated ^{129}Xe chemical shift (**Figure 3.3,**

Paper 5). Similar contributions and role of the dynamic solvent were also predicted for Xe atom dissolved in benzene in **Paper 6**.

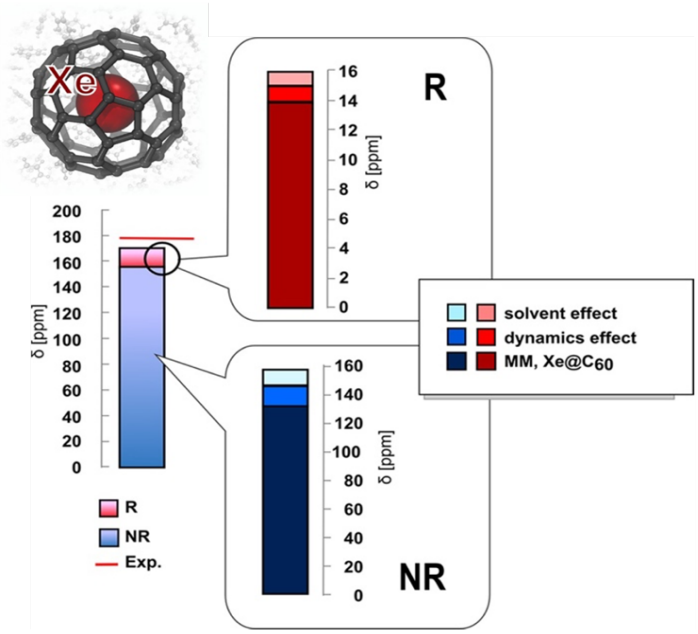

Figure 3.3: Individual physical contributions to ^{129}Xe chemical shifts in Xe@C_{60}. R= relativistic, NR = nonrelativistic. Adopted from **Paper 5**.

The role of various contribution is illustrated in **Figure 3.3**. The final computational protocol thus combines a reliable hybrid DFT functional (BHandHLYP) with dynamical averaging the system including explicit dynamic solvent around the molecule as well as dynamically averaged relativistic corrections from BPPT theory. This protocol yielded a theoretical value of 173 ppm for ^{129}Xe NMR shift in Xe@C_{60}, in a sound agreement with the experimental value of 179 ppm. The journey from a simple static model to a complex multi-scale simulation protocol established a robust and physically justified framework for predicting the NMR properties of confined Xe atom, that is relevant to the future experimental studies. It can be mentioned that **Paper 5** was highlighted on the cover page of the Journal of Computational Chemistry.

In **Paper 7,** we asked the question, how important is dynamics of the cage for ^{13}C NMR in pristine fullerene cage, C_{70}. We investigated influence of different physical effects on ^{13}C NMR spectrum in this system. A new finding was that vibrational and dynamical effects are relatively large in the gas phase (up to 9 ppm for individual carbon shifts) but are effectively damped in solvent (~ 2 ppm for individual shifts). Inclusion of dynamics effects enabled to qualitatively reproduce the temperature dependence of the experimental ^{13}C NMR spectrum of $C_{70,}$ although the differences in carbon shifts among various temperatures predicted computationally were an order of magnitude larger than experimental ones. Overall, the dynamical effects were found less important for ^{13}C shifts (**Paper 7**).

3.3. Ratcheting Rotation or Speedy Spinning: Effect of Temperature-Dependent Dynamics on EPR Spectra in $Sc_3C_2@C_{80}$

In 2003, Prof. Michael Mehring (Uni Stuttgart) presented us with a peculiar ^{45}Sc electron paramagnetic resonance (EPR) spectra of what was then assumed to be $Sc_3@C_{82}$ system. In particular, the observed spectra featured a resolved 22-line spectrum at 300 K and a single doublet spectrum at 100 K, see **Figure 3.4b.** This is in contrast with the typical situation, where lower temperatures lead typically to more resolved spectra. At that time, our attempts to reproduce the experimental spectra were unsuccessful.

In 2005, the ^{13}C NMR studies revealed that the molecule characterized by EPR spectra was not $Sc_3@C_{82}$ but $Sc_3C_2@I_h(7)$-C_{80} system.[20] This was based on presence of only two ^{13}C NMR signals in NMR spectrum, pointing to highly symmetric $I_h(7)$-C_{80} cage. Using correct structure, our calculations in **Paper 8** revealed that $Sc_3C_2@I_h(7)$-C_{80} is a chemically and dynamically rather interesting system. It features the C_2^{3-} carbon 'stick', that is fast librating amidst the triangle of the three Sc^{3+} atoms, while the cage accepts six electrons, being formally C_{80}^{6-}. While the interaction between the C_2^{3-} stick and Sc atoms is almost purely of electrostatic nature, the Sc atoms themselves are confined at certain distances from the cage walls, and 'breathe' with the cage during the cage vibrations. Initial, very short AIMD dynamics in **Paper 8** revealed, that the triangle defined by three Sc atoms swings along the hexagon-belt of the C_{80}

cage, while the C_2^{3-} librates fast through the plane defined by this triangle. However, static calculations and dynamical modelling over a short trajectory were not able to reproduce all of the features of the experimental EPR spectra in **Figure 3.4b**.

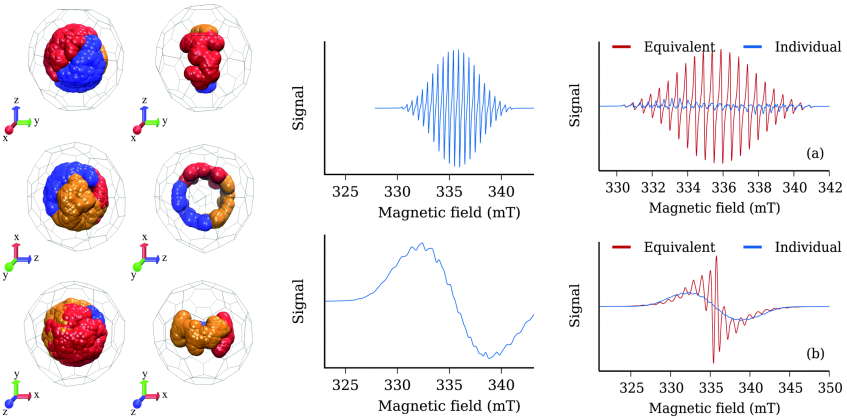

(a) **(b)** **(c)**

Figure 3.4: (a) Illustration of internal dynamics in $Sc_3C_2@C_{80}$ at 300K (left) and 100 K (right). The red, blue, and yellow colors correspond to individual Sc atoms. **(b)** Experimental and **(c)** simulated EPR spectra at 300 and 100 K. In **(c)** Red color corresponds to simulation with equivalent Sc atoms and blue considering non-equivalent Sc atoms. Adopted from **Paper 9**.

More comprehensive first-principles modelling in **Paper 9** enabled longer trajectories and suggested that the enclosed cluster exhibits peculiar dynamics, that can explain the temperature dependence of the EPR spectra, **Figure 3.4a**. While at low temperature the endohedral moiety undergoes ratcheting 2D motion along the equatorial belt of the C_{80} cage, at high temperature the motion is no longer restricted to a single plane. To test earlier assumptions, models featuring different equivalence of the three ^{45}Sc nuclei and either effectively isotropic or anisotropic parameter tensors were considered.

The main experimental EPR observations were reproduced by the present simulations (**Figure 3.4c**): a well-resolved 22-line spectrum arises

from isotropic and equivalent, rotationally averaged ^{45}Sc atoms at high temperature (300 K). In contrast, a broad line shape results from inequivalent metal centers with anisotropic hyperfine tensors at low temperature (100 K). **Paper 9** presents another example of importance of the dynamics in understanding fullerene moleculear properties.

3.4 'Chasing' Fullerenes with Optical Spectroscopy: Magnetic Circular Dichroism and Nuclear Spin Circular Dichroism in Fullerenes

The identification and characterization of fullerenes and their derivatives can be challenging due to the existence of multiple isomers with similar properties. While standard methods like X-ray diffractometry and NMR are invaluable, they can be limited by amount of sample typically available. Owing to the complicated preparation of fullerenes and endofullerenes, they are typically characterized first by mass spectra that only reveal stoichiometry and by UV-Vis-NIR spectroscopy, for which tiny amounts are sufficient.

In **Papers 10 and 11,** we demonstrated that Magnetic Circular Dichroism (MCD)[21] can be an interesting alternative to absorption spectroscopy. MCD spectroscopy measures the differential absorption of left- and right-circularly polarized light in the presence of a static magnetic field. Because the resulting signal can be either positive or negative, we observe couplets (derivative-like positive/negative features) instead of broad peaks and MCD spectra are thus more detailed than the electron absorption ones.[21] This may particularly help in fullerenes where absorption signals are often very broad.

In **Paper 10**, we measured and calculated experimental and theoretical absorption and MCD spectra in C_{60} and C_{70} to demonstrate the capability of MCD to provide distinct spectra for fullerene molecules. **Figure 3.5** illustrates the distinctive features of MCD spectra vs the absorption ones as well as the capability of DFT to reproduce the large part of the experimental MCD and absorption spectra. Requiring tiny amounts of the sample, the MCD technique thus appears as a useful technique for detailed fullerene studies.

Methodology established in **Paper 10** was applied to chlorofullerenes and their isomers in **Paper 11**. MCD spectra of $C_{60}Cl_6$,

$C_{70}Cl_{10}$ and $C_{60}Cl_{24}$ were measured and interpreted using a sum-over-state (SOS) protocol exploiting time dependent density functional theory (TDDFT). We have shown, that unlike for plain absorption, the MCD spectra exhibited easily recognizable features specific for each chlorinated molecule.

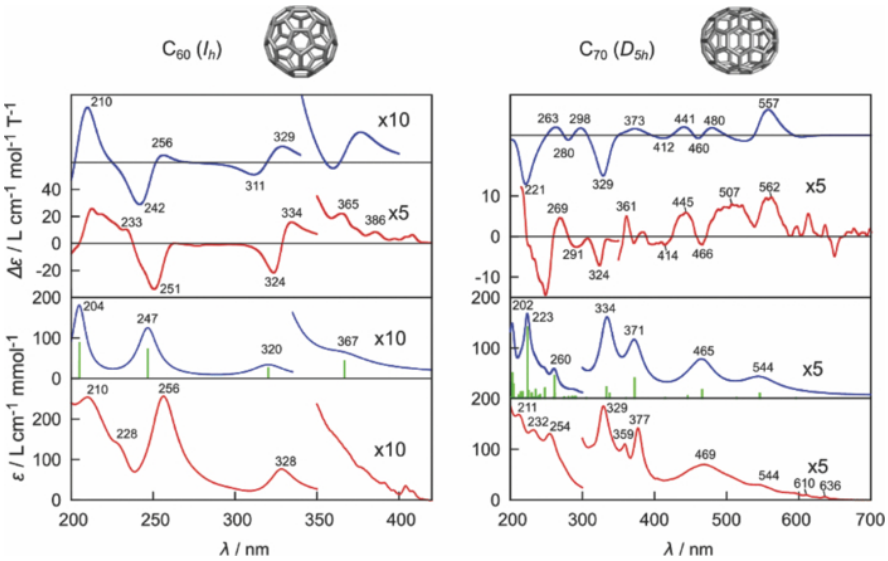

Figure 3.5: Calculated (blue upper, B3LYP/6-31G*) and experimental (red, lower) MCD (Δε) and absorption (ε) spectra of C_{60} and C_{70}. Line positions and intensities are indicated for calculated absorption in green. Adopted from **Paper 10**.

The TDDFT simulations provided a reasonable basis for interpretation of the most prominent spectral features. Notably, finer vibrational structure of the electronic bands was observed at longer wavelengths. **Paper 11** thus further confirmed the usefulness MCD in fullerene identification.

Nuclear Spin-Induced Circular Dichroism (NSCD) was formulated by Dr. Juha Vaara and coworkers in 2014.[22] In NSCD, a collective magnetization of atomic nuclei within a sample is used to induce circular dichroism in a light beam passing through it. While mathematically similar

to MCD, the two phenomena are physically distinct. The MCD effect is caused by the global Zeeman interaction of the molecule with an external magnetic field. In NSCD, the effect arises from local hyperfine interactions between electrons and the magnetic moments of nuclei. This distinction gives NSCD the exciting potential for local, nucleus-specific spectroscopic information, similar to NMR. An NSCD experiment would involve first magnetizing the nuclei (for example, using standard NMR equipment) and then measuring the differential absorption of light passing through the sample.

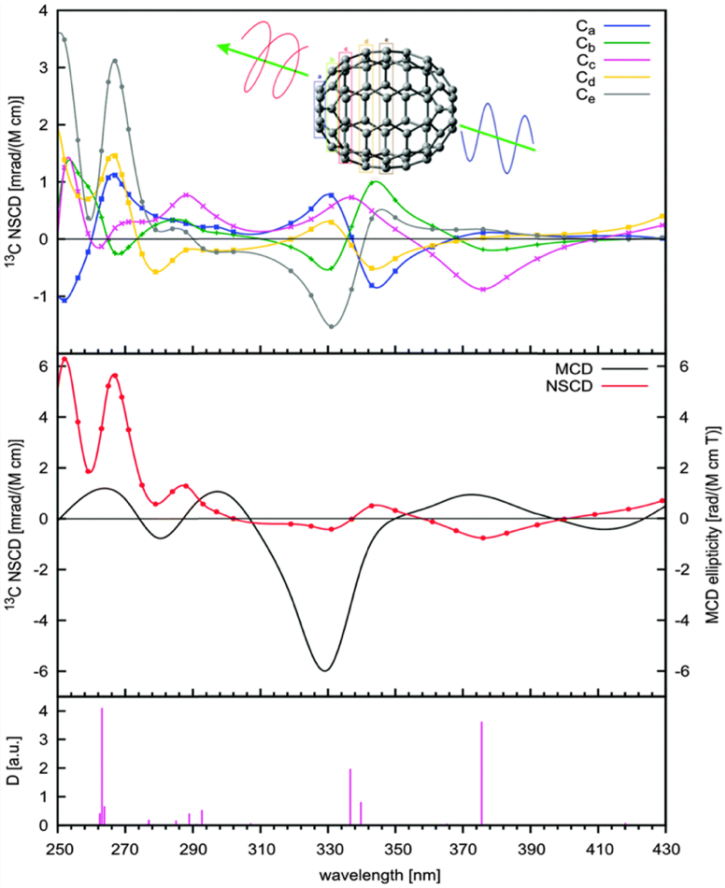

Figure 3.6: The calculated ^{13}C NSCD for the C_a–C_e nuclear sites (B3LYP/def2-SVP, upper panel) and the MCD (B3LYP/6-31G*, middle

panel) in C_{70}. The total ^{13}C NSCD signal (middle panel) is obtained as a sum of the signals for C_a–C_e. The excitation wavelengths and transition dipole strengths (B3LYP/def2-SVP) are shown in the bottom panel. Adopted from **Paper 12.**

When these individual signals are summed according to their degeneracy, they produce a total NSCD spectrum for the molecule that is, again, different from its MCD spectrum, middle panel in **Figure 3.6**. The ability to resolve signals from inequivalent nuclear sites demonstrates that NSCD could provide a new, high-resolution observable for the experimental identification of chemical compounds. However, the experiment has proven to be more complicated than anticipated. Despite the predictions, NSCD experiment has not been experimentally reported to date.

4. Unveiling Exotic Chemical Bonding in Fullerenes

4.1. Actinide–Actinide Bonding in Endohedral Fullerenes

While covalent metal-metal bonds are common for d-block elements, bonds between two actinide (An) atoms are rare. So far, the An–An bonds have been experimentally confirmed only for U_2 and Th_2 systems in the gas-phase, and, recently, in the interior of endohedral fullerenes.

Back in 2015, when we started our investigation, little was known about the An–An bonds in endohedral fullerenes. The only hint then was existence of mass-spectrometric evidence for various diactinide fullerenes, such as $U_2@C_{60}$ and $U_2@C_{80}$,[23] together with theoretical prediction of multiple U–U bonding in $U_2@C_{60}$ by Wu and Lu,[24] that was questioned by Infante and Gagliardi, who argued that the U–U bonding in $U_2@C_{60}$ is an artifact of the small cavity in C_{60}. They argued that in larger cavities, e.g. of C_{70} and C_{84}, the two uranium atoms preferentially bind the internal walls and the U−U bonding no longer exists.[25]

To resolve these ambiguities, we investigated theoretically (employing the BP86/def2-SVP 'model chemistry') the $U_2@C_n$ (n = 60, 70, 80, 84, 90) systems in **Paper 13** and concluded that the bonding between two actinides, though forcefully driven by the confinement of the cage is 'real' in context of electronic structure predictions and analysis of electron

density (MO, NBO, QTAIM, spin density). We pointed out the formation of one-electron-two-center (OETC) bonds between the two uranium atoms and coined the U–U bonding as *unwilling bonding* in which the $5f^3$ shell of the formally U^{3+} localizes between the two U atoms to minimize the electrostatic repulsion between the charged actinide atoms. The predicted $U_2@I_h(7)$-C_{80} molecule was later characterized experimentally.[26] This encouraged us to pursue further studies.

In 2020 (**Paper 14**) we investigated actinide-actinide bonding in $An_2@D_{5h}(1)$-C_{70}, $An_2@I_h(7)$-C_{80}, and $An_2@D_{5h}(1)$-C_{90} (An = Ac–Cm) series of endohedral metallofullerenes. We showed that a number of the studied $An_2@C_{70}$ and $An_2@C_{80}$ systems feature actinide-actinide bonds with strong 5f-character. The σ, π, and even *δ*
OETC bonds were predicted at BP86/def2-SVP level for various systems.

The study was highlighted in C&N News.[27] In there, however, we got criticism from Prof. Gagliardi saying that 'the calculations should include accounting for electron correlation and relativistic effects in a more comprehensive way.' That gave us the push to go more deeply in the theoretical description.

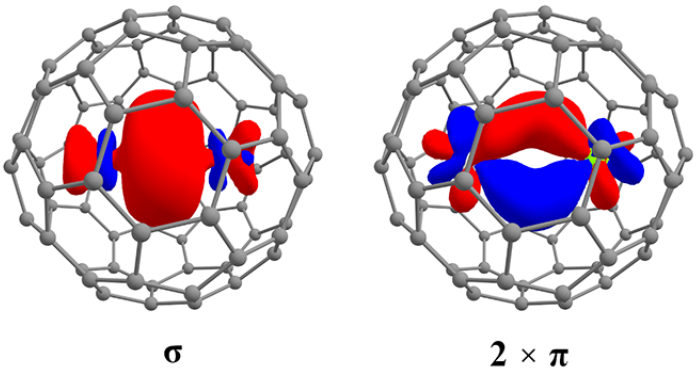

Figure 4.1 Illustration of typical An–An one-electron-two-center bonding orbitals in $An_2@C_{80}$ systems. Adopted from **Paper 14**.

Another push was provided by finding that $Th_2@I_h(7)$-C_{80} predicted by us in **Paper 14** was later characterized experimentally.[9]

Multireference wave-function calculations reported therein predicted a closed-shell singlet $^1Th_2@C_{80}$ system with a closed-shell $\boldsymbol{\sigma}$ Th–Th bond (similar to that in **Figure 4.1**) in contrast with our DFT BP86/def2SVP prediction of high-spin triplet $^3Th_2@C_{80}$ with two one-electron-two-center bonds, **Figure 4.1**. The conflict between the DFT and multireference description of $Th_2@C_{80}$ finally initiated a comprehensive methodological benchmark to establish a reliable computational protocol for actinide-actinide bonding in fullerenes.

In **Paper 15**, a study was undertaken by us to compare the performance of a selected number of DFT functionals, spanning GGAs, meta-GGAs, hybrids, and range-separated hybrids, against the high-level multireference CASPT2 method, which accounts for static and dynamic electron correlation and was treated as the reference. The experimentally characterized $Th_2@I_h(7)$-C_{80} and $U_2@I_h(7)$-C_{80} systems served as benchmark molecules. The results of this study revised our understanding of the An–An bonding in fullerenes. Main results were:

1. The electronic structure of $Th_2@C_{80}$ system was found to be single-reference in character. Most DFT functionals performed reasonably well, predicting a Th–Th bond length and a delocalization index DI(Th−Th) in the range of 0.6−0.8 in a good agreement with the CASPT2 benchmark value of 0.7. This confirmed the presence of a conventional single Th–Th bond. However, most of the DFT functionals would incorrectly put the ground state singlet above the triplet, **Figure 4.2a**.
2. For $U_2@C_{80}$, the study revealed a dramatic failure of the common DFT functionals. The CASPT2 benchmark calculation yielded a DI(U−U) of only 0.07, indicating a marginal, essentially non-covalent interaction. In contrast, GGA functionals like BP86 overestimated the bond order by more than a factor of ten with DI(U−U) ~ 1.0. While hybrid functionals reduced this overestimation, only the range-separated functionals provided a qualitatively better picture, though still overestimating the interaction DI(U–U) ~ 0.2. Also, the analysis of the CAS wavefunction revealed that various spin-states of the system are

almost degenerate from septet to singlet (**Figure 4.2b**) which means, that the two uranium atoms are non-interacting.

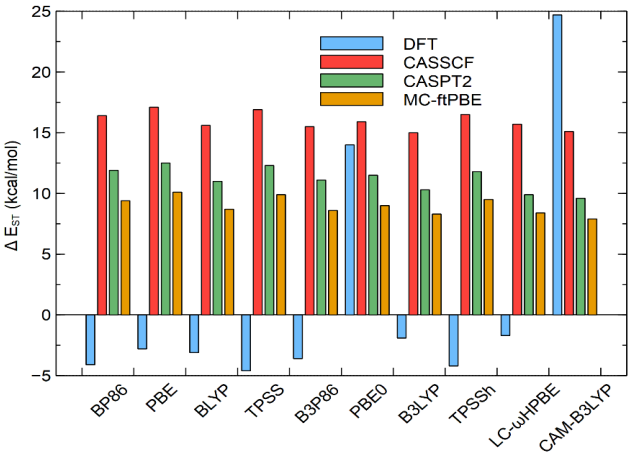

(a)

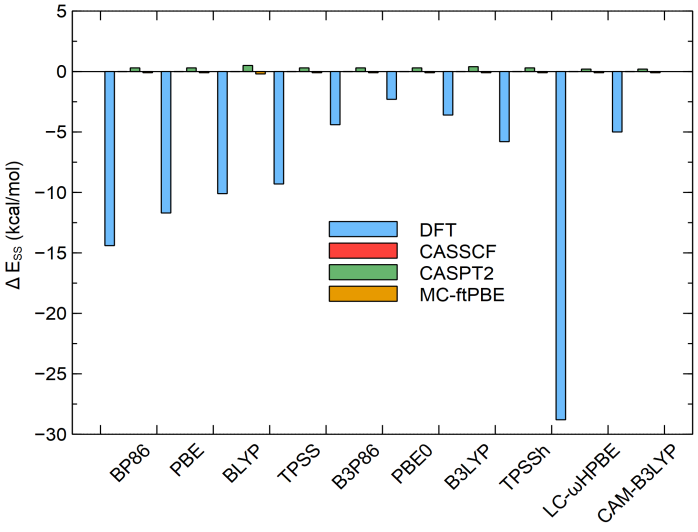

(b)

Figure 4.2: Predicted energy differences between spin states **(a)** E(^{3}Th$_2$@C$_{80}$) - E(^{1}Th$_2$@C$_{80}$) **(b)** E(^{7}U$_2$@C$_{80}$) - E(^{1}U$_2$@C$_{80}$). The DFT calculation of E(^{1}U$_2$@C$_{80}$) uses broken-symmetry approximation. Adopted from **Paper 15**.

This rigorous re-evaluation demonstrated that the initial concept of U–U bond in $U_2@C_{80}$ was an artifact of using an inadequate theoretical method (DFT BP86) for a system with a strong multireference character. We have shown that at accurate CASPT2 level, the An–An bonding still exists, even for uranium, when in smaller cages, like C_{60}.

As one of the results of **Paper 15** have revisited the diactinide fullerenes from **Paper 14** and corrected the DFT data. We have shown that U–U bonding exists in C_{60} with DI(U–U) ~ 1.5, and Th–Th bonding exists also in C_{70} and C_{80} DI(Th–Th) ~ 0.7. Similarly, the Pa–Pa bond even exists in C_{80} with DI(Pa–Pa) ~ 0.7.

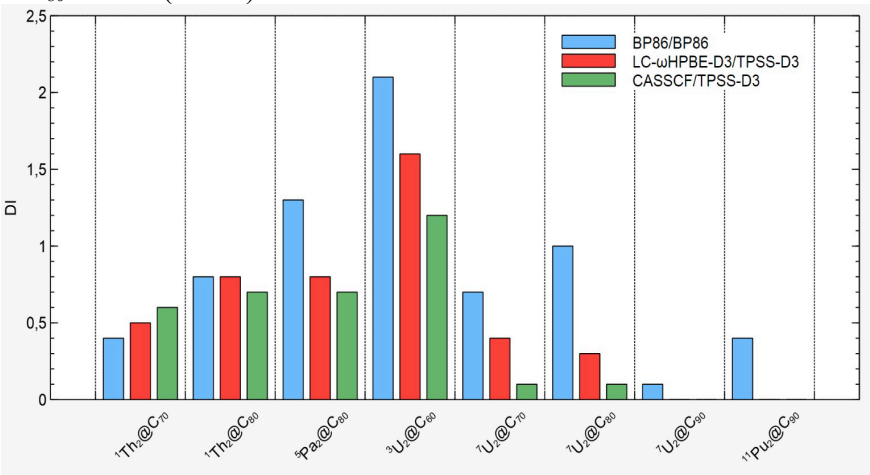

Figure 4.3: The predicted An–An delocalization index (DI) for selected compounds at various levels of theory for density and geometry.

4.2. Charge Depletion Bonding Inside Fullerenes

What happens when neutral molecular systems are enclosed in a fullerene, for example HF···H_2O system, a prototype of Lewis acid-base pair? Experiments revealed that the FH···OH_2 hydrogen bond substantially shortens (1.5 vs 1.7 Å) while the H–F bond slightly elongates upon encapsulation of the cluster in C_{70}, see geometries in **Figure 4.4.**[8] The authors speculated that it is due to the confinement of the small interior of fullerene that makes these molecules to interact stronger.

In **Paper 16** we have shown, that this is not the case, and situation is more delicate. Our calculations revealed that the shortening of FH···OH_2 inside the cavity of C_{70} is a result unique LP_F–π_{cage} interactions with a

charge-depletion character in the bonding region, unlike usual LP–π bonds, **Figure 4.4c**. The LP_F–π interactions induce elongation of the H–F bond in HF, that leads to a more acidic HF and resulting shorter FH···OH_2 contact in (HF·H_2O)@C_{70}. This is further demonstrated on (HF·H_2O)@C_{90} system. Even in a larger cavity of C_{90}, the FH···OH_2 bond is shorter than in the gas phase HF···H_2O system (1.6 vs 1.7 Å). As a proof of concept, investigation of analogous L_1L_2@C_n ($L_{1/2}$ = HF, H_2O, and NH_3; n = 70, 80, 90) systems revealed additional examples of the charge-depletion bonding in **Paper 16.**

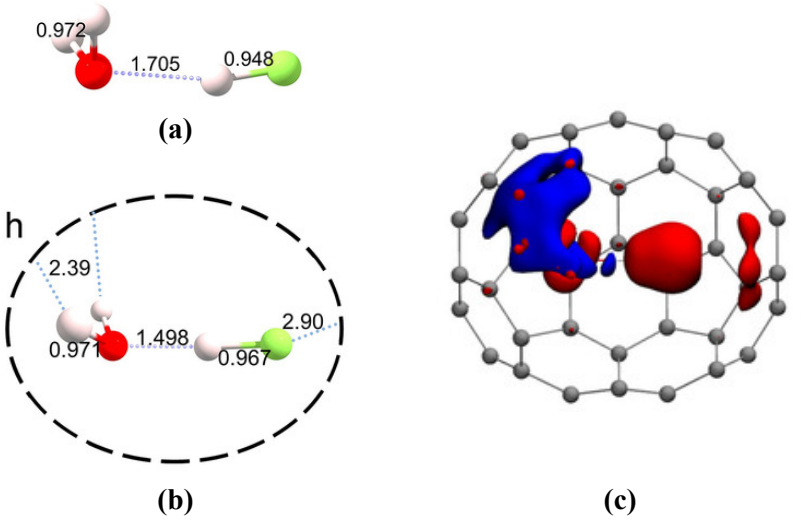

Figure 4.4: Calculated B97D3/def2-SVP structures : **(a)** gas-phase HF·H_2O and **(b)** (HF·H_2O)@C_{70}. **(c)** Charge-depleted bonding in (HF·H_2O)@C_{70} red color represents depletion of electron density for system in cage. Adopted from **Paper 16**.

4.3. F_2^-@C_{60}^+ : Fullerene 'Single-Molecule Crystal'

Normally, in endohedral fullerenes, the cage is either neutral or accepts electrons from enclosed metals or clusters. But what happens when we enclose a strong electron acceptor inside a fullerene cage, such as F_2? We have predicted (**Paper 17**) that F_2 molecule enclosed in C_{60} fullerene oxidizes the fullerene cage and stabilizes itself as F_2^- anion. Notably, the interaction between F_2^- and C_{60}^+ is predicted to be of almost purely

electrostatic nature, making this molecule a 'single-molecule crystal'. Additionally, $F_2^-@C_{60}^+$ is a rare example of an endohedral fullerene, where the enclosed moiety is negatively charged while the fullerene is oxidized. We also predicted that $F_2^-@C_{60}^+$ may easily reduce to $F_2^-@C_{60}$ with an electron on enclosed F_2. We also tested if other halogens would behave similarly in various fullerene cages, however, only F_2 oxidizes fullerene cages from inside (unpublished results).

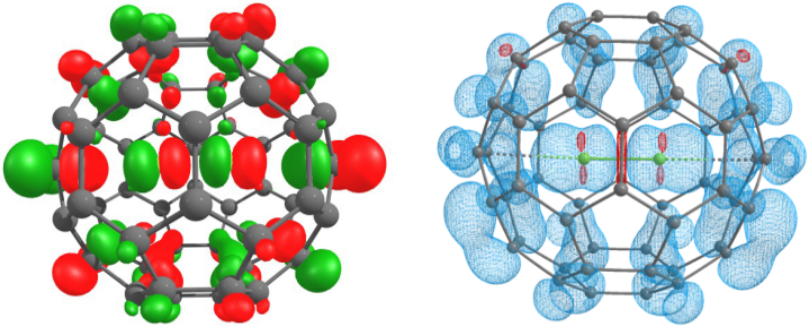

Figure 4.4: (a) $\sigma_u^*(F_2)$–based SOMO of $^3F_2@C_{60}$. (b) Spin density in the ground-state $^3F_2@C_{60}$. Adopted from **Paper 17**.

4.4. London Formula For Endohedral Systems

During the $Xe@C_{60}$ studies we have come around an interesting question. What would be the London formula for endohedral systems? London has derived his approximative formula for estimation of the dispersion interaction between two separated subsystems A and B forming in A···B system as:[28]

$$E_{disp} \leq 0.75\, I_A I_B\, (\alpha_A\, \alpha_B)\, R^{-6} \qquad (1)$$

where I is the ionization potential, α the dipole polarizability, and R the intermolecular distance, all in atomic units (a.u.). The problem with endohedral systems is that original London formula is defined for separated A···B systems but not for enclosed A@B systems, where R_{AB} cannot be uniquely defined.

In **Paper 18,** we developed London-like formula for dispersion energy in endohedral A@B systems. This formula's key novelty is the 'irregular polarizability,' $\alpha^{-2}(B)$, for the outer host system, which uses

an r^{-2} radial operator but has no explicit dependence on the host's radius. The endohedral London formula has then similar form as the original London formula but the $\alpha^{-2}(B)$ is used for B.

The concept was further generalized in **Paper 19** by Dr. Wang by expressing the interaction energy in A@B system using one-center expansion. The interaction energy can then be calculated from the properties of individual monomers. The developed theoretical model provides a tool for dissecting the energetics of endohedral systems and estimating the different physical contributions involved, i.e. electrostatic, induction, and dispersion. While offering valuable physical insight and qualitative estimates, the work confirms that direct supramolecular calculations remain the benchmark for high accuracy.

5. Rational Design of Fullerene-Based Molecular Electronics

5.1. MX@C_{70}: Electric Field-Driven Single-Molecule Switch

Molecular electronics aims at miniaturization of electronics by replacing macroscopic circuit components with single molecules featuring similar functions. Since the Aviram and Ratner introduced the first examples of molecular diodes,[29] various molecular components, such as wires, rectifiers, switches, and transistors have been proposed and fabricated.[30]

Our contribution to molecular electronics lies in proposed concept of electric-field driven single-molecule switch (**Paper 20**) that can function as molecular memristor (**Papers 21-22**) and, when spin-filtering function is added, as a molecular spinristor (**Paper 23**).

Molecular switch is a molecule that can be reversibly switched between two or more stable states. The stimuli for switching can be, for example light, temperature, pH, or electric field (EF). In our pilot work, **Paper 20**, we proposed *electric-field driven single-molecule switch* that is based on MX@C_{70} endohedral fullerenes, where MX is a dipolar system enclosed in a fullerene cage, such as LiCl or CaO. In such a system, an external electric field (EEF) allows to flip the MX dipole between two local minima, LM and LM', **Figure 5.1a**. The minima are separated by an energy barrier, that is removed when applied EEF is large enough, **Figure 5.1b**.

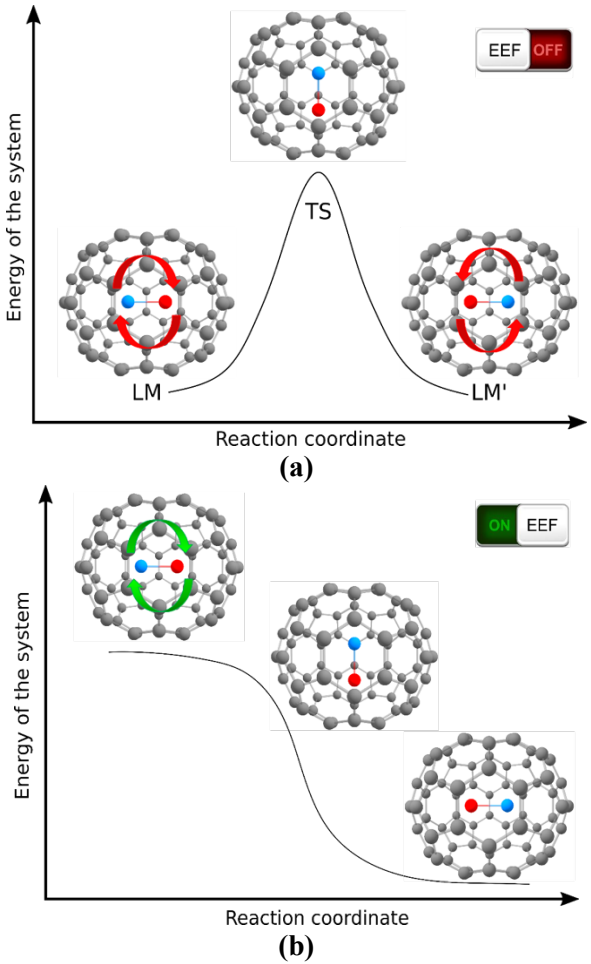

Figure 5.1 : The principle of an MX@C_{70} molecular switch (EEF stands for external electric field). (**a**) MX@C_{70} with two local minima (LM and LM') separated by a transition state (TS) with an energy barrier. (**b**) Upon application of external voltage, one of the local minima becomes unstable. This leads to the rotation of MX between LM and LM' (or LM' to LM), and thus to the switching of the system's polarity and conductivity. Adopted from **Paper 20**.

Our theoretical predictions confirmed that for certain MX systems, external electric field (EEF) is capable to switch the dipolar MX there and back, if the barrier is not too large. We concluded that EEF can encode the information in the switch, which makes it a potential system for a single molecule memory.

5.2. From Molecular Switch To Molecular Memristor

The results in **Paper 20** provided proof of concept for the EF-driven switch but were not satisfactory enough to have ambitions towards practical applications. First, the intrinsic switching barrier could be overcome only for systems with a low barrier, some systems would not switch even with large EEF. To help the MX@C_{70} switch to overcome the barrier, we proposed a four-electrode setup in **Paper 21** (**Figure 5.2a**). We demonstrated that perpendicular external field further stabilizes the TS and thus helps to remove the barrier for switching the dipole inside the fullerene cage. This is illustrated in **Figure 5.2b.**

More importantly, in **Paper 21,** we also proposed to read the state of the switch (LM and LM' in **Figure 5.1**) by connecting the MX@C_{70} system to electrodes (**Figure 5.2c**) and *measuring its conductivity*. Indeed, Non-Equilibrium Green Function (NEGF) DFT calculations of MX@C_{70} system connected to golden electrodes have shown differential conductivity for LM and LM' minima (**Figure 5.2d**). Thus, when the MX@C_{70} switch is connected to electrodes, a large potential on electrodes can be used for switching the MX and thus changing the state and conductivity, and low potential can be used for measuring the conductivity, and thus reading the state of the system.

We originally called the MX@C_{70} system as a *fullerene switching diode*. It occurred to us only later, that it actually functions in similar manner as a *memristor*. A memristor is an electronic component that retains information about the past current flow or the voltage previously applied to it.[31] Typical property of a memristor is a hysteresis on I/V curves. Indeed, in MX@C_{70} the switching of MX leads to a hysteresis on I/V curves) that resembles those of bulk memristors, **Figure 5.3c**. We illustrated function of MX@C_{70} memristor in popularizing YouTube video (https://youtu.be/z2h_hdvn1cm).

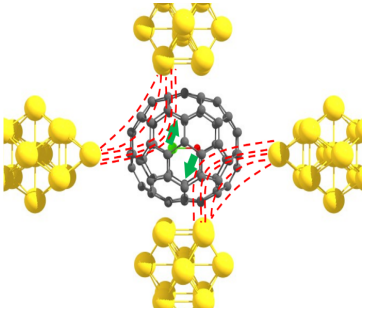

(a)

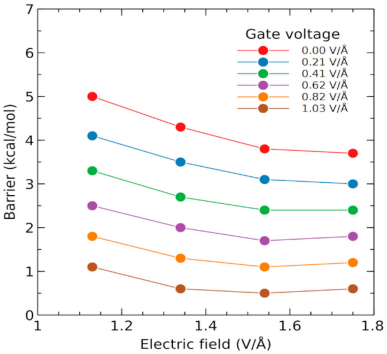

(b)

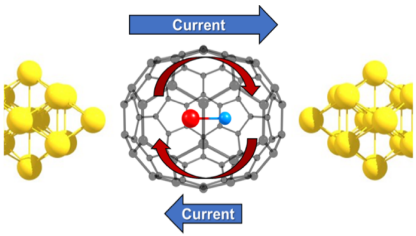

(c)

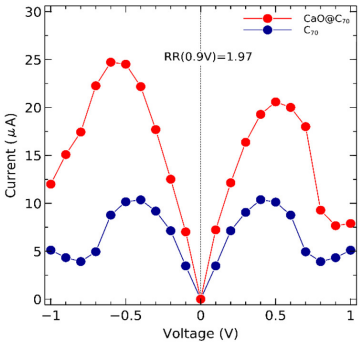

(d)

Figure 5.2: **(a)** The four-electrode setup in which the source-drain voltage (V_{SD}) is applied horizontally and the gate voltage (V_G) is perpendicular to the V_{SD}. **(b)** The predicted response of the switching barrier to the external fields in LiCl@C_{70}. **(c)** When MX@C_{70} is connected to electrodes it acts as a memristor. **(d)** Differential conductivity of the two local minima of CaO@C_{70}. Adopted from **Paper 21.**

Notably, the memristor concepts, predicted by us in **Paper 21** *have been observed experimentally* by other groups on similar molecules after our predictions. Specifically, Gd@C_{82} and Sc_2C_2@C_{88} molecules, coined as a molecular electret,[12] and logic in-memory device,[13] respectively, work on the principles that we have predicted computationally. The later system was

fabricated in a device that performs logical operations and, notably, works at room temperatures.

In **Paper 22**, we further developed the concept of a fullerene memristor on series of various $MX@C_{70}$ molecules (M = alkali and alkaline earth metals, X = halogens and chalcogens) and we discovered and formulated simple rules for deriving potentially relevant systems. Among others, anticipated correlation between the M-X interatomic distance and intrinsic switching barrier was found, as well as the correlation between the size of the dipole moment of MX and switching response. We also performed a method calibration on energetics of $MX@C_{70}$ systems, concluding that a DZP-quality basis set is well-converged for geometry, and TZP-quality basis set is well converged for energetics and barrier. PBE0 functional performed best among ten tested functionals in comparison to single-point DLPNO-CCSD(T)/aug-cc-TZVP benchmark.

The proposal of a single-molecule memristor is one of the most important contributions of this thesis. A memristor has the unique advantage of functioning both as a memory and as a processing unit. In contemporary computer architecture, processing (CPU) and memory (RAM) are physically separate. Communication between the CPU and RAM represents a major bottleneck in current technology, limiting both speed and energy efficiency.

Memristive computing offers an attractive alternative, combining memory and processing within a single unit and operating with low energy consumption. Moreover, when properly interconnected in circuits, memristors can emulate the behavior of neurons and neural networks. This enables neuromorphic computing, a paradigm that seeks to build hardware and software mimicking the structure and function of the neural networks and human brain. Single-molecule memristors therefore hold significant promise for future frontier research at the interface of molecular electronics, memristive materials, and neuromorphic computing.

5.3. Spinristor: A Swiss-Army Knife Of Molecular Electronics

A spin filter is a device through which the spin-up and spin-down electrons pass at different rates. It is important for spintronics, which differs from classical electronics in that, that electron spins are used as an additional degree of freedom with different implications and applications.

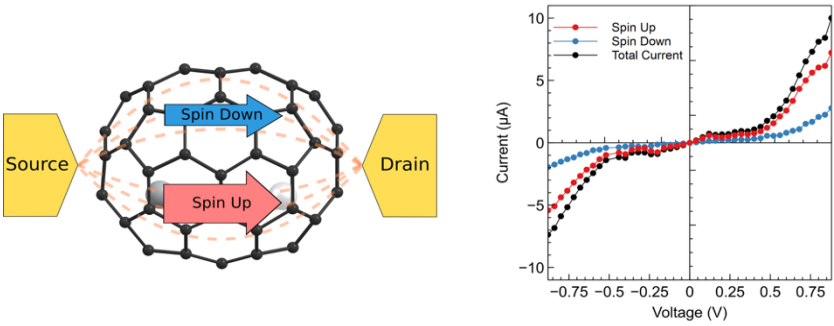

(a)

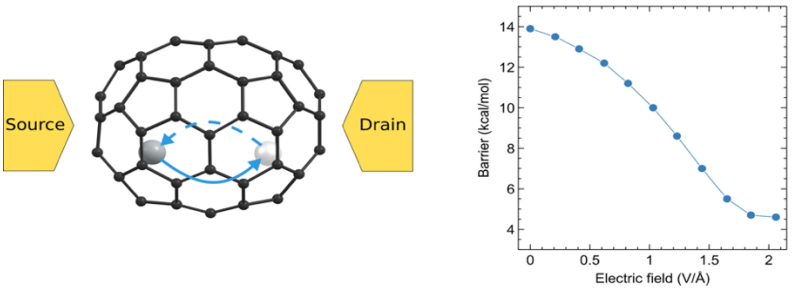

(b)

Figure 5.4: The concept of Ti@C_{70} spinristor. Panel **(a)** illustrates spin-filtering function. Panel **(b)** illustrates the switching by electric field. Adopted from **Paper 23**.

The integration of a spin-filtering function into a molecular switch defines a spinristor, a component, that can switch between different conductive modes for spin-up and spin-down electrons. This we achieved in **Paper 23** by utilizing a metal ion with an open-shell electronic structure enclosed in a fullerene, such as in the Ti@C_{70} model system, **Figure 5.4.** In Ti@C_{70} the Ti ion inside the cage features open-shell triplet structure with two unpaired electrons on Ti atom. This leads to inherent differential spin-conductivity for spin-up and spin-down electrons, **Figure 5.4a**. The positions of the Ti ion inside the cage can be switched by a higher voltage

applied, **Figure 5.4b**. The different positions of Ti inside the cage (we found a tri-stable system) feature different spin-up/spin-down conductivity owing different orbital energy levels of spin-up and spin-down molecular orbitals in individual isomers.

When it comes to practical application, spinristors may suffer from the same disadvantage as molecular magnet, i.e., it has to maintain the spin. The experimental setup then requires low temperatures, or other means to keep the magnetization. The experimental proof and applications of a spinristor thus remain to be seen.[32]

6. Conclusions

6.1. Summary of Research Journey

This dissertation has summarized a computational research journey through the world of endohedral fullerenes. It illustrated a journey from fundamental scientific inquiry to rational design. The narrative began with the use of encapsulated noble gas atoms as sensitive spectroscopic probes, which required the development of increasingly sophisticated computational models to unravel the complex interplay of symmetry, relativity, and dynamics that govern their NMR chemical shifts. This foundational understanding of the endohedral environment was then leveraged to explore the cage as a unique nanolaboratory capable of fostering exotic chemical bonding, leading to the correction of computational protocols on actinide-actinide interactions and the discovery of unprecedented bonding motifs, such as the actinide-actinide bonds, charge-shifting bonding, or the 'single-molecule crystal' $F_2^-@C_{60}^+$. Finally, theory was applied to the *in silico* design and validation of novel molecular devices: first, electric field-driven fullerene molecular switch, then a fullerene molecular memristor, culminating in the proposal of the spinristor, a fundamentally new spintronic component.

6.2. Key Scientific Contributions

The work presented in this dissertation has made several key contributions to the field of computational chemistry and nanoscience:

- **Elucidation of NMR Shielding Mechanisms:** A definitive, symmetry-based mechanism was formulated to explain the puzzling NMR chemical shifts observed in endohedral helium fullerenes. We showed that the effect is linked to high symmetry of fullerene cages, allowing or quenching of paramagnetic orbital couplings due to the symmetry rules.
- **Development of a Multi-Scale Simulation Protocols:** A rigorous, 'physics-first' computational protocol was developed and validated for accurately predicting the ^{129}Xe NMR spectroscopy in confined Xe systems. This multi-scale approach systematically integrates DFT, relativistic theory, and explicit-solvent molecular dynamics, demonstrating that all three components are essential for quantitative accuracy.
- **Refinement and Discovery in Actinide Bonding:** Through meticulous methodological benchmarking against high-level multireference calculations. Refined methodology subsequently enabled the reliable predictions of An–An bonds in fullerenes. Th–Th and Pa–Pa bonding was predicted, in addition to the previously reported U–U bonding in small cages, such as in $U_2@C_{60}$. Some of our theoretical predictions have been experimentally confirmed later, such as the $Th_2@C_{80}$ system.
- **Concept of Fullerene Memristor and Its Rational Design:** We conceptualized the $MX@C_{70}$ electric field-driven fullerene molecular switch, that can act as a molecular memristor. A rational design for a fullerene-based molecular memristor was demonstrated. This included the initial concept, the validation of 'write' and 'read' mechanisms by employing EEF and DFT-NEGF calculations, and a large-scale computational screening that yielded concrete, generalizable engineering rules correlating guest properties (bond length, dipole moment) with device characteristics (switching voltage).
- **Concept of the Spinristor:** A novel spintronic device, the spinristor, was conceptualized theoretically. This work represents a paradigm shift from mimicking classical components to designing

new functionalities from first principles, integrating memristive switching and spin-filtering into a single molecule.

6.3. Outlook and Future Directions

The computational discoveries presented herein lay the groundwork for exciting future research at the intersection of chemistry, physics, and materials science. The immediate challenge lies in the experimental realization of the proposed molecular devices. This will require significant advances in the targeted synthesis of specific endohedral fullerenes and in the fabrication and addressing of single-molecule junctions. From a theoretical perspective, future work should focus on several key areas. The dynamics of the switching process in memristors and spinristors, occurring on picosecond timescales, could be investigated using ab initio molecular dynamics to provide a more complete picture beyond the static energy barriers. Modeling the complex interface between the molecular component and the macroscopic electrodes, including the role of different linker chemistries and surface interactions, remains a significant challenge. For the spinristor, exploring a wider range of guests and fullerene cages could lead to devices with tailored magnetic properties, higher spin-filtering efficiencies, or multi-state logic capabilities. Ultimately, the journey documented in this dissertation underscores the great potential of endohedral fullerenes as versatile building blocks for the technologies of the future, a potential that will continue to be unlocked through the close partnership of computational modeling and experimental innovation

7. References

(1) Kroto, H. W.; Heath, J. R.; O'Brien, S. C.; Curl, R. F.; Smalley, R. E. C_{60}: Buckminsterfullerene. *Nature* **1985**, *318* (6042), 162–163. https://doi.org/10.1038/318162a0.

(2) Popov, A. A.; Yang, S.; Dunsch, L. Endohedral Fullerenes. *Chem. Rev.* **2013**, *113* (8), 5989–6113. https://doi.org/10.1021/cr300297r.

(3) Hou, Y.; Kong, X. Endometallofullerenes in the Gas Phase: Progress and Prospect. *Inorganics* **2024**, *12* (3), 68. https://doi.org/10.3390/inorganics12030068.

(4) Cai, W.; Zhang, M.; Echegoyen, L.; Lu, X. Recent Advances in Endohedral Metallofullerenes. *Fundam. Res.* **2025**, *5* (2), 767–781. https://doi.org/10.1016/j.fmre.2023.12.004.

(5) Sinha, S.; Sanfo, K.; Dallas, P.; Kumar, S.; Porfyrakis, K. Process Parameter Optimisation for Endohedral Metallofullerene Synthesis via the Arc-Discharge Method. *Inorganics* **2024**, *12* (2), 38. https://doi.org/10.3390/inorganics12020038.
(6) Bloodworth, S.; Whitby, R. J. Synthesis of Endohedral Fullerenes by Molecular Surgery. *Commun. Chem.* **2022**, *5* (1), 121. https://doi.org/10.1038/s42004-022-00738-9.
(7) Saunders, M.; Jimenez-Vazquez, H. A.; Bangerter, B. W.; Cross, R. J.; Mroczkowski, S.; Freedberg, D. I.; Anet, F. A. L. ^{3}He NMR: A Powerful New Tool for Following Fullerene Chemistry. *J. Am. Chem. Soc.* **1994**, *116* (8), 3621–3622. https://doi.org/10.1021/ja00087a067.
(8) Zhang, R.; Murata, M.; Wakamiya, A.; Shimoaka, T.; Hasegawa, T.; Murata, Y. Isolation of the Simplest Hydrated Acid. *Sci. Adv.* **2017**, *3* (4), e1602833. https://doi.org/10.1126/sciadv.1602833.
(9) Zhuang, J.; Morales-Martínez, R.; Zhang, J.; Wang, Y.; Yao, Y.-R.; Pei, C.; Rodríguez-Fortea, A.; Wang, S.; Echegoyen, L.; De Graaf, C.; Poblet, J. M.; Chen, N. Characterization of a Strong Covalent Th^{3+}–Th^{3+} Bond inside an $I_h(7)$-C_{80} Fullerene Cage. *Nat. Commun.* **2021**, *12* (1), 2372. https://doi.org/10.1038/s41467-021-22659-2.
(10) Zhang, X.; Zhang, J.; Liu, D.; Zhang, W. Functionalized Fullerene: A Key Driver for High Performance Inverted Perovskite Solar Cell. *J. Energy Chem.* **2025**, *111*, 30–50. https://doi.org/10.1016/j.jechem.2025.07.050.
(11) Castro, E.; Garcia, A. H.; Zavala, G.; Echegoyen, L. Fullerenes in Biology and Medicine. *J. Mater. Chem. B* **2017**, *5* (32), 6523–6535. https://doi.org/10.1039/C7TB00855D.
(12) Zhang, K.; Wang, C.; Zhang, M.; Bai, Z.; Xie, F.-F.; Tan, Y.-Z.; Guo, Y.; Hu, K.-J.; Cao, L.; Zhang, S. A Gd@C_{82} Single-Molecule Electret. *Nat. Nanotechnol.* **2020**, *15* (12), 1019–1024.
(13) Li, J.; Hou, S.; Yao, Y.-R.; Zhang, C.; Wu, Q.; Wang, H.-C.; Zhang, H.; Liu, X.; Tang, C.; Wei, M.; Xu, W.; Wang, Y.; Zheng, J.; Pan, Z.; Kang, L.; Liu, J.; Shi, J.; Yang, Y.; Lambert, C. J.; Xie, S.-Y.; Hong, W. Room-Temperature Logic-in-Memory Operations in Single-Metallofullerene Devices. *Nat. Mater.* **2022**, *21* (8), 917–923. https://doi.org/10.1038/s41563-022-01309-y.
(14) Syamala, M. S.; Cross, R. J.; Saunders, M. ^{129}Xe NMR Spectrum of Xenon Inside C_{60}. *J. Am. Chem. Soc.* **2002**, *124* (21), 6216–6219. https://doi.org/10.1021/ja012676f.
(15) Saunders, M.; Jiménez-Vázquez, H. A.; Cross, R. J.; Poreda, R. J. Stable Compounds of Helium and Neon: He@C_{60} and Ne@C_{60}. *Science* **1993**, *259* (5100), 1428–1430. https://doi.org/10.1126/science.259.5100.1428.
(16) Saunders, M.; Jimenez-Vazquez, H. A.; Cross, R. J.; Billups, W. E.; Gesenberg, C.; Gonzalez, A.; Luo, W.; Haddon, R. C.; Diederich, F.;

Herrmann, A. Analysis of Isomers of the Higher Fullerenes by ^{3}He NMR Spectroscopy. *J. Am. Chem. Soc.* **1995**, *117* (36), 9305–9308. https://doi.org/10.1021/ja00141a023.
(17) Sternfeld, T.; Saunders, M.; Cross, R. J.; Rabinovitz, M. The Inside Story of Fullerene Anions: A ^{3}He NMR Aromaticity Probe. *Angew. Chem. Int. Ed.* **2003**, *42* (27), 3136–3139. https://doi.org/10.1002/anie.200351429.
(18) Boventi, M.; Mauri, M.; Simonutti, R. ^{129}Xe: A Wide-Ranging NMR Probe for Multiscale Structures. *Appl. Sci.* **2022**, *12* (6), 3152. https://doi.org/10.3390/app12063152.
(19) Schröder, L. Xenon for NMR Biosensing – Inert but Alert. *Phys. Med.* **2013**, *29* (1), 3–16. https://doi.org/10.1016/j.ejmp.2011.11.001.
(20) Iiduka, Y.; Wakahara, T.; Nakahodo, T.; Tsuchiya, T.; Sakuraba, A.; Maeda, Y.; Akasaka, T.; Yoza, K.; Horn, E.; Kato, T.; Liu, M. T. H.; Mizorogi, N.; Kobayashi, K.; Nagase, S. Structural Determination of Metallofullerene Sc_3C_{82} Revisited: A Surprising Finding. *J. Am. Chem. Soc.* **2005**, *127* (36), 12500–12501. https://doi.org/10.1021/ja054209u.
(21) Fusè, M.; Mazzeo, G.; Ghidinelli, S.; Evidente, A.; Abbate, S.; Longhi, G. Experimental and Theoretical Aspects of Magnetic Circular Dichroism and Magnetic Circularly Polarized Luminescence in the UV, Visible and IR Ranges: A Review. *Spectrochim. Acta. A. Mol. Biomol. Spectrosc.* **2024**, *319*, 124583. https://doi.org/10.1016/j.saa.2024.124583.
(22) Vaara, J.; Rizzo, A.; Kauczor, J.; Norman, P.; Coriani, S. Nuclear Spin Circular Dichroism. *J. Chem. Phys.* **2014**, *140* (13), 134103. https://doi.org/10.1063/1.4869849.
(23) Guo, T.; Diener, M. D.; Chai, Y.; Alford, M. J.; Haufler, R. E.; McClure, S. M.; Ohno, T.; Weaver, J. H.; Scuseria, G. E.; Smalley, R. E. Uranium Stabilization of C_{28}: A Tetravalent Fullerene. *Science* **1992**, *257* (5077), 1661–1664. https://doi.org/10.1126/science.257.5077.1661.
(24) Wu, X.; Lu, X. Dimetalloendofullerene $U_2@C_{60}$ Has a U−U Multiple Bond Consisting of Sixfold One-Electron-Two-Center Bonds. *J. Am. Chem. Soc.* **2007**, *129* (7), 2171–2177. https://doi.org/10.1021/ja067281g.
(25) Infante, I.; Gagliardi, L.; Scuseria, G. E. Is Fullerene C_{60} Large Enough to Host a Multiply Bonded Dimetal? *J. Am. Chem. Soc.* **2008**, *130* (23), 7459–7465. https://doi.org/10.1021/ja800847j.
(26) Zhang, X.; Wang, Y.; Morales-Martínez, R.; Zhong, J.; Graaf, C. de; Rodríguez-Fortea, A.; Poblet, J. M.; Echegoyen, L.; Feng, L.; Chen, N. $U_2@I_h(7)$-C_{80}: Crystallographic Characterization of a Long-Sought Dimetallic Actinide Endohedral Fullerene. *J. Am. Chem. Soc.* **2018**. https://doi.org/10.1021/jacs.7b10865.
(27) Lemonick, S. *Caged actinides form unusual bonds in simulations*. Chemical & Engineering News. https://cen.acs.org/physical-

chemistry/computational-chemistry/Caged-actinides-form-unusual-bonds/98/i34.
(28) London, F. Zur Theorie und Systematik der Molekularkräfte. *Z. Für Phys.* **1930**, *63* (3), 245–279. https://doi.org/10.1007/BF01421741.
(29) Aviram, A.; Ratner, M. A. Molecular Rectifiers. *Chem. Phys. Lett.* **1974**, *29* (2), 277–283. https://doi.org/10.1016/0009-2614(74)85031-1.
(30) Xiang, D.; Wang, X.; Jia, C.; Lee, T.; Guo, X. Molecular-Scale Electronics: From Concept to Function. *Chem. Rev.* **2016**, *116* (7), 4318–4440. https://doi.org/10.1021/acs.chemrev.5b00680.
(31) Strukov, D. B.; Snider, G. S.; Stewart, D. R.; Williams, R. S. The Missing Memristor Found. *Nature* **2008**, *453* (7191), 80–83. https://doi.org/10.1038/nature06932.
(32) Shao, Q.; Wang, Z.; Zhou, Y.; Fukami, S.; Querlioz, D.; Chua, L. O. Spintronic Memristors for Computing. *Npj Spintron.* **2025**, *3* (1), 16. https://doi.org/10.1038/s44306-025-00078-z.

List of Publications Included in the Dissertation

P1: **Straka, M.***; Vaara, J. Density Functional Calculations of ^{3}He Chemical Shift in Endohedral Helium Fullerenes: Neutral, Anionic, and Di-Helium Species. *J. Phys. Chem. A*, **2006**, *110*, 12338–12341. https://doi.org/10.1021/jp0638991. **IF**: 2.8 **Scopus: 28**

P2: Štěpánek, P.; Bouř, P.; **Straka, M.*** Assignment of the He@C_{84} Isomers in Experimental NMR Spectra Using Density Functional Calculations. *Chem. Phys. Lett.* **2010**, *500* (1–3), 54–58. https://doi.org/10.1016/j.cplett.2010.09.061. **IF**: 3.1 **Scopus: 17**

P3: Vícha, J.*; Vaara, J.*; **Straka, M.** The Essential Role of Symmetry in Understanding ^{3}He Chemical Shifts in Endohedral Helium Fullerenes. *Phys. Chem. Chem. Phys.* **2023**, *25* (15), 10620–10627. https://doi.org/10.1039/D3CP00256J. **IF**: 2.9 **Scopus: 6**

P4: Straka, M.*; Lantto, P.; Vaara, J. Toward Calculations of the ^{129}Xe Chemical Shift in Xe@C_{60} at Experimental Conditions: Relativity, Correlation, and Dynamics. *J. Phys. Chem. A*, **2008**, *112*, 2658–2668. https://doi.org/10.1021/jp711674y.
IF: 2.8 **Scopus: 60**

P5: Standara, S.; Kulhánek, P.; Marek, R.; **Straka, M.*** ^{129}Xe NMR Chemical Shift in Xe@C_{60} Calculated at Experimental Conditions: Role of the Relativity, Dynamics, and Explicit Solvent. *J. Comp. Chem.*, **2013**, *34*, 1890. https://doi.org/10.1002/jcc.23334. **IF**: 4.8 **Scopus: 18**

P6: Standara, S.; Kulhánek, P.; Marek, R.; Horníček, J.; Bouř, P.; **Straka, M.*** Simulations of ^{129}Xe NMR Chemical Shift of Atomic Xenon Dissolved in Liquid Benzene. *Theor. Chem. Acc.*, **2011**, *129*, 677–684. https://doi.org/10.1007/s00214-011-0930-z. **IF**: 1.5 **Scopus: 24**

P7: Kaminský,* J.; Buděšínský, M.; Taubert, S.; Bouř, P.; **Straka, M.*** Fullerene C_{70} Characterization by ^{13}C NMR and the Importance of the Solvent and Dynamics in Spectral Simulations. *Phys. Chem. Chem. Phys.*, **2013**, *15*, 9223–9230. https://doi.org/10.1039/c3cp50657f.
IF: 2.9 **Scopus: 34**

P8: Taubert, S.; **Straka, M.**; Pennanen, T. O.; Sundholm,* D.; Vaara, J. Dynamics and Magnetic Resonance Properties of $Sc_3C_2@C_{80}$ and Its Monoanion. *Phys. Chem. Chem. Phys.*, **2008**, *10*, 7158–7168. https://doi.org/10.1039/b811032h. **IF**: 2.9 **Scopus: 30**

P9: Roukala, J.; **Straka, M.**; Taubert, S.; Vaara, J.; Lantto, P.* Ratcheting Rotation or Speedy Spinning: EPR and Dynamics of $Sc_3C_2@C_{80}$. *Chem. Comm.*, **2017**, *53*, 8992–8995. https://doi.org/10.1039/c7cc04695b. **IF**: 4.2 **Scopus: 8**

P10: Štěpánek, P.; **Straka, M.**; Andrushchenko, V.; Bouř,* P. Communication: Fullerene Resolution by the Magnetic Circular Dichroism. *J. Chem. Phys.* **2013**, *138* (15). https://doi.org/10.1063/1.4802763.
IF: 3.1 **Scopus: 18**

P11: Štěpánek, P.; **Straka, M.**; Šebestík, J.; Bouř,* P. Magnetic Circular Dichroism of Chlorofullerenes: Experimental and Computational Study. *Chem. Phys. Lett.* **2016**, *647*, 117–121. https://doi.org/10.1016/j.cplett.2016.01.047.
IF: 3.1 **Scopus: 8**

P12: **Straka, M.***; Štěpánek, P.; Coriani, S.; Vaara, J.* Nuclear Spin Circular Dichroism in Fullerenes: A Computational Study. *Chem. Commun.* **2014**, *50* (96), 15228–15231. https://doi.org/10.1039/C4CC07271E. **IF**: 4.2 **Scopus: 9**

P13: Foroutan-Nejad, C.; Vícha, J.; Marek, R.; Patzschke, M.; **Straka, M.*** Unwilling U–U Bonding in $U_2@C_{80}$: Cage-Driven Metal–Metal Bonds in Di-Uranium Fullerenes. *Phys. Chem. Chem. Phys.* **2015**, *17* (37), 24182–24192. https://doi.org/10.1039/C5CP04280A. **IF**: 2.9 **Scopus: 53**

P14: Jaroš, A.; Foroutan-Nejad, C.*; **Straka, M.*** From ***π***-bonds without **σ**-bonds to the Longest Metal-Metal Bond Ever: A Survey on Actinide-Actinide Bonding in Fullerenes. *Inorg. Chem.*, **2020**, *59*, 12608. https://doi.org/10.1021/acs.inorgchem.0c01713. **IF**: 4.7 **Scopus: 25**

P15: Jaroš, A.; **Straka, M.*** Unravelling Actinide–Actinide Bonding in Fullerene Cages: A DFT *versus Ab Initio* Methodological Study. *Phys. Chem. Chem. Phys.* **2023**, *25* (45), 31500–31513. https://doi.org/10.1039/D3CP03606E. **IF**: 2.9 **Scopus: 6**

P16: Jaroš, A.; Badri, Z.; Bora, P. L.; Bonab, E. F.; Marek, R.; Straka, M.*; Foroutan-Nejad, C.* How Does a Container Affect Acidity of Its Content: Charge-Depletion Bonding Inside Fullerenes. *Chem. Eur. J.* **2018**, *24* (17), 4245. https://doi.org/10.1002/chem.201706017. **IF**: 5.5 **Scopus: 26**

P17: Foroutan-Nejad, C.*; **Straka, M**.*; Fernández, I.*; Frenking, G.* Buckyball Difluoride F_2^-@ C_{60}^+ — a Single-Molecule Crystal. *Angew. Chem. Int. Ed.* **2018**, *57* (42), 13931–13934. https://doi.org/10.1002/anie.201809699. **IF**: 16.9 **Scopus: 27**

P18: Pyykkö, P.; Wang, C.; **Straka, M.**; Vaara, J. A London-Type Formula for the Dispersion Interactions of Endohedral A@B Systems. *Phys. Chem. Chem. Phys.* **2007**, *9* (23), 2954–2958. https://doi.org/10.1039/B704695B. **IF**: 2.9 **Scopus: 47**

P19: Wang, C.; **Straka, M**.; Pyykkö, P. Formulations of the Closed-Shell Interactions in Endohedral Systems. *Phys. Chem. Chem. Phys.* **2010**, *12* (23), 6187–6203. https://doi.org/10.1039/B922808J. **IF**: 2.9 **Scopus: 29**

P20: Foroutan-Nejad, C.; Andrushchenko, V.; **Straka, M.*** Dipolar Molecules inside C_{70}: An Electric Field-Driven Room-Temperature Single-Molecule Switch. *Phys. Chem. Chem. Phys.* **2016**, *18* (48), 32673–32677. https://doi.org/10.1039/C6CP06986J. **IF**: 2.9 **Scopus: 51**

P21: Jaroš, A.; Bonab, E. F.; **Straka, M**.*; Foroutan-Nejad, C.* Fullerene-Based Switching Molecular Diodes Controlled by Oriented External Electric Fields. *J. Am. Chem. Soc.* **2019**, *141* (50), 19644–19654. https://doi.org/10.1021/jacs.9b07215. **IF**: 15.6 **Scopus: 71**

P22: Tučková, L.; Jaroš, A.; Foroutan-Nejad, C*.; **Straka, M.*** A Quest for Ideal Electric Field-Driven MX@ C_{70} Endohedral Fullerene Memristors: Which MX Fits the Best? *Phys. Chem. Chem. Phys.* **2023**, *25* (20), 14245–14256. https://doi.org/10.1039/D3CP01149F.
IF: 2.9 **Scopus: 8**

P23: Jaroš, A.; Sasar, M.; Tučková, L.; Bonab, E. F.; Badri, Z.; **Straka, M.***; Foroutan-Nejad, C.* Spinristor: A Spin-Filtering Memristor. *Adv. Electron. Mater.* **2023**, 2300360. https://doi.org/10.1002/aelm.202300360. **IF**: 5.3 **Scopus: 2**